

Effect of modes of metal transfer and microstructure on corrosion behavior of welded modified ferritic stainless steel in acidic environments

Manidipto Mukherjee · Tapan Kumar Pal

Received: 7 August 2012 / Accepted: 26 November 2012 / Published online: 22 December 2012
© Springer Science+Business Media Dordrecht 2012

Abstract The effects of modes of metal transfer, i.e., short-circuit (SC) and spray (S) modes in single-pass gas metal arc welding of modified ferritic stainless steel using two types of austenitic stainless steel filler metals on microstructure as well as corrosion behavior of weld metal and high-temperature heat-affected zone (HTHAZ), were investigated. The results show that primary solidification modes (PSM) of the welds were exclusively dependent upon the $\text{Cr}_{\text{eq}}/\text{Ni}_{\text{eq}}$ ratio of the respective welds. However, the amount of grain boundary austenite and martensite transformation in the welds were solely dependent upon the mode of metal transfer and the extent of cooling rate. Regarding the corrosion mechanism, grain boundary corrosion (GBC) behavior of welds and HTHAZ relied on the microstructural changes along the grain boundary due to the variation in mode of metal transfer. The results show that S-mode resisted grain boundary corrosion of the welds and both GBC as well as pitting corrosion of the HTHAZ. On the other hand, SC-mode improved only pitting corrosion resistance of the welds. Between the filler wires used, 316L welds, in general, provided better corrosion resistance compared with 308L welds.

Keywords Ferritic Stainless steel · Welding · Polarization · Grain boundary corrosion · Pitting corrosion

1 Introduction

Ferritic stainless steel (FSS) with 11–12 % Cr has been developed to fill the gap between high cost austenitic stainless steels (ASS) and the rust-prone carbon steels as low cost utility stainless steels. These modified FSS grades are now commonly used in the coal mining industry for bulk transport of coal and gold, for cane and beet sugar processing equipment, road and rail transport, power generation, petrochemical, pulp and paper industries etc. In fact, the use of these steels in the past few years has been increased markedly with their successful applications in passenger vehicles, coaches, buses, trucks, freight, and passenger wagons [1, 2]. Furthermore, FSS is a candidate material in comparatively less severe corrosion atmosphere for chemical processing equipment, furnace parts, cold end (below 600 °C) automotive exhaust parts such as mufflers and a tail pipe, heat exchangers, petroleum refining equipment, storage vessels, electrical appliances, solar water heaters, and household appliances [3]. They are particularly more applicable in caustic and chloride environments [4]. However, the excessive presence of Cl^- , SO_4^{2-} , SO_3^{2-} , CH_3COOH , CO_3^{2-} , and HCO_3^- in different environments may cause corrosion and degrade the performance of the material [3–5]. For example, the environment in the cold end automotive exhaust part, sometimes, became quite corrosive due to higher concentrations of Cl^- , SO_4^{2-} , SO_3^{2-} etc., in exhaust gases and condensed water [4, 5].

The use of such FSS in engineering applications obviously is related to its weldability. Since gas metal arc welding (GMAW) is commonly used for making various structural components, in addition to mechanical properties, corrosion properties of different zones such as weld metal and HAZ at least should match with base metal for structural integrity.

M. Mukherjee · T. K. Pal (✉)
Metallurgical and Material Engineering Department,
Welding Technology Center, Jadavpur University,
Kolkata 700032, India
e-mail: tkpal.ju@gmail.com

M. Mukherjee
e-mail: m.mukherjee.ju@gmail.com

Formations of martensite and high-temperature embrittlement in HAZ are inherent problems associated with FSS [3, 4]. When matching ferritic stainless steels are used as filler metals, coarse columnar grains are produced in cast weld metal, as the material does not undergo phase transformation between room temperature and melting point. Such grain growth not only reduces toughness and ductility, but also decreases corrosion resistance [6, 7]. On the other hand, an austenitic filler metal is found to be the most suitable from mechanical properties as well as corrosion resistance point of view [6–8]. Gooch and Davey [8] recommended 309L as the most suitable filler although 308L and 310 are also suitable. In order to attain maximum benefit of GMAW for a given application, suitable welding consumables and welding conditions must be selected on the basis of not only mechanical properties, but also corrosion properties.

The corrosion behavior of stainless steel (SS) weldments is the goal of a wide number of studies. Perhaps the most common problem encountered in SS weldments has been associated with sensitization in the heat affected zone (HAZ) leading to intergranular corrosion (IGC) or grain boundary corrosion (GBC) and pitting corrosion. According to the previous research articles [9, 10], IGC and/or GBC mechanism of FSS is similar to that of ASS. However, according to Tuthill [11], Sedriks [12], and White [13], the FSS is more susceptible to GBC than ASS due to its lower solubility of carbon and nitrogen, which facilitate precipitation of carbides and other intermetallic phases at grain boundaries during heating in the sensitization temperature range, typically 400–900 °C. Again, the corrosion behavior of FSS welds also depends upon the type of inclusion (such as sulfides, oxides etc.) and phase fractions (i.e., volume fraction of ferrite, austenite, and martensite) present in the microstructure [9, 10, 14–16]. In the last two decades, several models have been proposed to explain the sensitization mechanism of stainless steel; however, the chromium depletion model (CDM) is the most widely accepted [17, 18]. On the other hand, little research on the pitting corrosion in the HAZ of welded FSS has been reported [19, 20]. The failure of the thin adherent and passive oxide films induces localized corrosion-like pitting due to sensitized microstructure and residual stresses [20]. However, two models, i.e., Point defect model (PDM) and mixed-conduction model (MCM), which are proposed by the previous investigators [14, 21] are the most applicable for explaining both IGC and pitting corrosion.

Although the corrosion phenomena associated with the HAZ have been considered to be more significant than weld metal, the cast structure of the weld metal poses additional problems related to corrosion. The micro-segregation of chromium–molybdenum and the high ferrite content at the fusion line as well as unmixed sub-zone, where the metal melted without mixing with filler metal,

modify corrosion behavior [15, 16]. In addition, two-phase microstructure formation, i.e., δ -ferrite and grain boundary austenite (GBA), in the weld metal using austenitic filler wire should be taken into account because of their susceptibility to attack in a corrosive environment [22]. It is worth mentioning here that besides the GBC and pitting corrosion, interdendritic corrosion and galvanic corrosion are rarely found in FSS weldments [20–22].

With regard to welding, the heat input and cooling rate are two important parameters affecting the corrosion resistance because they could induce segregation of alloying elements and formation of chromium-depleted zones [20, 23]. The cooling rate during welding has provided to be a factor that influences the desensitization of the ferrite phase through chromium back diffusion into the depleted regions during slow cooling [24]. This suggests that heat input which invariably controls cooling rate is a parameter that can influence the sensitization of FSS. For a given material, the higher the heat input, the slower the cooling rate. The susceptibility of 11–12 % chromium type EN1.4003 ferritic stainless steels to sensitization during continuous cooling after welding at low heat input was investigated by Greeff et al. [25], and it was found that welding at low-heat inputs can suppress the transformation of ferrite to austenite as the HAZ cools through the dual phase (austenite + ferrite) region during welding. However, with an increase in heat input, the cooling rate is reduced and more austenite forms in the HAZ. According to Mukherjee and Pal [26], the presence of austenite along the grain boundary also depends upon the modes of metal transfer. The spray mode of metal transfer (S-mode) induces more amount of grain boundary austenite in the weld metal and this grain boundary austenite ultimately transforms to lath martensite due to high-heat input and slower cooling associated with this mode; whereas, in short-circuit mode (SC-mode), the cooling rate being faster, suppresses the formation of grain boundary austenite and thus lath martensite. It is to be mentioned here that the sensitization can be prevented by the presence of enough austenite to eliminate continuous ferrite–ferrite grain boundaries [25]. Even the presence of grain boundary martensite in FSSs increased the resistance to sensitization under different heat input conditions [24]. Since FSS is being welded extensively with gas metal arc welding (GMAW) using austenitic filler wire under different modes of metal transfer, operating mode should be optimized for a given filler wire to achieve the improved corrosion properties of the weldments. However, the effect of modes of metal transfer in GMAW process using different austenitic filler wires on the corrosion behavior of FSS weldments is hardly available in the literature. Therefore, in order to improve the life of various structural components made of FSS, it is crucial to find out the effects of distinctive

metallurgical changes that take place during welding on the corrosion behavior of weldments.

In this article, welding parameters were varied to operate with two different modes of metal transfer, i.e., short-circuit (SC-mode) and spray (S-mode) in GMAW process using two types of austenitic filler wires, i.e., 308L and 316L under Ar + 5 % CO₂ atmosphere. The aim was to study the effect of compositional and metallurgical changes in FSS weldments, induced by different modes of metal transfer using 308L and 316L ASS filler wire, on corrosion behavior in distinct environments, i.e., H₂SO₄ solution and NaCl solution. A series of electrochemical corrosion tests were conducted on weld metal (WM) and high-temperature heat-affected zone (HTHAZ) to examine the corrosion behavior of the FSS weldments.

2 Experimental procedure

2.1 Materials, specimen preparation and analysis

The base metals (BM) used in this investigation were rolled plates (as received) of 4-mm thickness SSP-409M grade-modified FSS sheets. The full penetration square butt joints with a root gap of 1.5 mm were prepared in GMAW process using two different austenitic filler metals such as 308L and 316L of 1.2 mm diameter, in single pass, without post weld heat treatment (PWHT). The chemical composition of the base plates and filler wires are given in Table 1. The welding operation conditions are presented in

Table 2. Selection of welding operation conditions was such that two different modes of metal transfer, i.e., short-circuit (SC) and spray (S) modes could be operated. To ascertain the two different modes of metal transfer, current and voltage were recorded by oscilloscope during each welding run (Fig. 1). The short-circuit mode (SC-mode), as shown in Fig. 1a, was identified as almost zero potential drop after a certain period of time, whereas almost constant potential drop in Fig. 1b indicates spray mode (S-mode). In the present study, spray mode was achieved at a current of 220 A, whereas short-circuit mode of metal transfer was obtained at a current level of 180 A as shown in Table 2. However, it is to be mentioned here that globular to spray mode was obtained at about 190–200 A in GMA welding with 1.2 mm diameter stainless steel electrode as reported by Lowke [27]. The variation in operating transition current level, from Lowke's observation, could be due to the different filler wires used.

In order to evaluate the chemical composition of welds, percentage dilution (%D_L) of base plate was calculated from the geometric characteristics of weld joints such as total area of weld deposit (A_{WD}), area of top (A_{TR}) and root (A_{RR}) reinforcement, area of base metal fusion (A_{BF}), and area of root gap (A_{RG}) as schematically shown in Fig. 2. The estimations of A_{WD}, A_{BF}, and D_L were determined as follows [28], and all the outcomes are given in Table 3:

$$A_{WD} = A_{RG} + A_{TR} + A_{BF} + A_{RR} \quad (1)$$

$$A_{BF} = A_{WD} - A_{RG} - A_{TR} - A_{RR} \quad (2)$$

$$D_L\% = A_{BF}/A_{WD} \times 100\% \quad (3)$$

Table 1 Chemical composition (wt%) of base metal and filler metals

Type	C (%)	Si (%)	Mn (%)	P (%)	S (%)	Cr (%)	Ni (%)	Mo (%)	Cu (%)	Nb (%)	N (%)
Base Metal	0.030	0.463	0.79	0.029	0.014	11.10	0.31	0.033	0.026	0.017	0.01
308L	0.015	0.53	1.68	0.012	0.03	19.53	9.26	0.117	0.082	0.026	0.053
316L	0.026	0.4	1.7	0.025	0.012	18.66	11	2.6	0.08	0.03	0.07

Table 2 Welding conditions and process parameters

Sl. no	Current (A)	Voltage (V)	WFS (m min ⁻¹)	WS (mm min ⁻¹)	HI (kJ mm ⁻¹)	Gas mixture	GFR (L min ⁻¹)	MTM
Process parameters for 308L filler wire								
SC1	180	26	6.00	500	0.40	Ar + 5 %CO ₂	16	Short
S1	220	28	7.00		0.52			Spray
Process parameters for 316L filler wire								
SC2	180	26	6.00	500	0.40	Ar + 5 %CO ₂	16	Short
S2	220	28	7.00		0.52			Spray

WFS wire feed speed, WS welding speed, HI heat input, GFR gas flow rate, MTM metal transfer modes

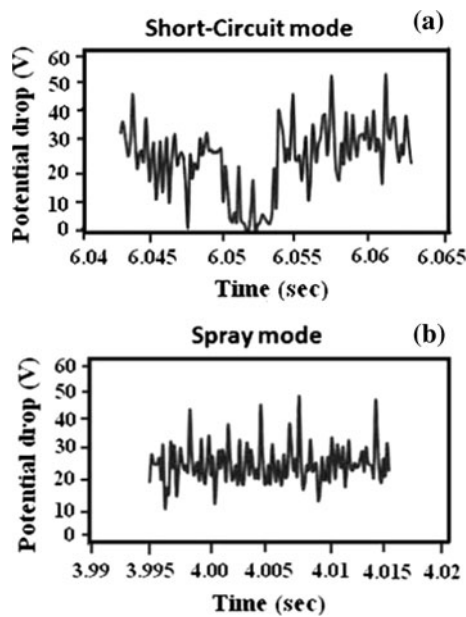


Fig. 1 Potential drop versus Time curves of **a** Short-circuit and **b** Spray modes of metal transfer

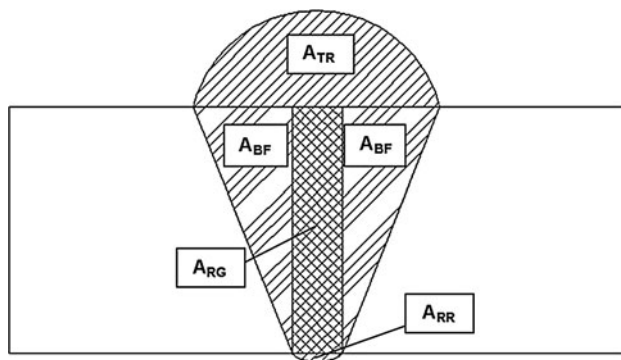


Fig. 2 Schematic representation of different locations in welded joint considered for graphical measurement of A_{WD} and A_{BF} used in dilution calculation

Table 3 Dilution calculations for different welds

Sample specification	SC1	S1	SC2	S2
A_{BF} (mm ²)	12.13	16.65	12.19	17.01
A_{WD} (mm ²)	27.36	35.46	27.78	36.2
D_L (%)	44.34	46.95	43.8	47

Weld metal compositions obtained from dilution were used to calculate the chromium equivalent (Cr_{eq}) and nickel equivalent (Ni_{eq}) values using the following equations [29] along with Cr_{eq}/Ni_{eq} ratio. All the end data are summarized in Table 4.

Table 4 Composition of different welds (wt%) derived from dilution and Cr_{eq} , Ni_{eq} , Cr_{eq}/Ni_{eq} ratio

Elements	SC1	S1	SC2	S2
C	0.021	0.022	0.028	0.028
Si	0.5	0.499	0.42	0.43
Mn	1.28	1.26	1.3	1.27
P	0.02	0.02	0.027	0.028
S	0.023	0.022	0.013	0.012
Cr	15.79	15.56	15.36	15.12
Ni	5.29	5.08	6.34	5.976
Mo	0.08	0.078	1.5	1.415
Cu	0.056	0.056	0.056	0.054
Nb	0.022	0.022	0.024	0.024
N	0.034	0.033	0.044	0.045
Cr_{eq}	16.63	16.40	17.50	17.20
Ni_{eq}	7.58	7.36	9.15	8.80
Cr_{eq}/Ni_{eq}	2.19	2.23	1.91	1.95

$$Cr_{eq} = wt\% Cr + wt\% Mo + 0.5(wt\% Nb) + 1.5(wt\% Si) \quad (4)$$

$$Ni_{eq} = wt\% Ni + 30(wt\% C) + 30(wt\% N) + 0.5(wt\% Mn) \quad (5)$$

The specimens for metallography comprising weld metal, HAZ, and base metal were prepared, polished using different grades of silicon carbide (emery) papers followed by final polishing in the disk polishing *m/c* using diamond compound (1- μ m particle size). The specimens were then etched with 10 ml hydrochloric acid, 0.5 g cupric chloride, and 10 ml ethanol for 10–15 s. Microstructural examination was carried out using a light optical microscope (Make: Carl ZEISS India Pvt. Ltd.; Model: Imager.A1m).

The XRD measurements were performed in a Rigaku X-ray diffractometer (made in Japan) using the monochromatic Cu K α radiation operated at 40 kV tube voltage and 30 kA tube current, with a scan rate of 1° per min, and 2 θ ranging from 40° to 100°. The specimens of 10 mm \times 10 mm \times 0.5 mm were prepared for XRD measurements.

The welded specimens were also examined under Transmission Electron Microscope (TEM) (Make: Philips Ltd., Netherlands; Model: CM-70) to observe the microstructure in greater detail. The specimens for TEM were prepared using a diamond cutter and fine grades of emery papers up to 0.1 mm followed by final thinning in chemical etching/thinning process up to 10 μ m.

2.2 Electrochemical measurements

The specimens of welds and HAZ were separately cold-mounted in epoxy resin. The surfaces of the specimens were ground with silicon carbide papers from 120 down to

1200 grade, washed with distilled water, degreased with acetone, and dried in air. In order to prevent the possibility of crevice corrosion during measurement, the interface between sample and resin was coated with a lacquer leaving an exposed surface area of 0.25 cm².

Electrochemical corrosion behavior of the specimens was investigated using potentiostatic anodic polarization measurements in 2 M H₂SO₄ and 1 M NaCl naturally aerated solutions. All the potentiostatic anodic polarization measurements were performed in a linear sweep voltammeter equipped with a standard one-compartment three-electrode cell. The reference electrode (RE) was Ag/AgCl, and the counter electrode was a standard platinum stick. All electrode potential values are referred to this reference electrode. The working electrodes were FSS specimens (weld and HTHAZ). All electrochemical measurements were made at room temperature (25 ± 2 °C) with an AUTOLAB model PGSTAT 30/302N potentiostat/galvanostat (computer controlled) using the general purpose electrochemical software (Gpes) version 4.9. The software determined the corrosion potential (E_{corr}), corrosion current (I_{corr}), and corrosion current density (i_{corr}) from the polarization curves using Tafel extrapolation method, and calculated the corrosion rates in mm/year.

Before anodic polarization, working electrodes were immersed in the electrolytes for at least 600 s for stabilization of the open-circuit potential (OCP). Polarization curves were measured at a potential range of −1000 mV (RE) to +2000 mV (RE). The scan rate of 10 mV s^{−1} was exercised during the polarization test. After each scan, the electrolytes were replaced. The specimens were polished after each experiment, rinsed in water, and washed with acetone to remove products that might form on the surface that could in turn affect the measurement. All tests were carried out in triplicate to ensure reliability, and a fairly good reproducibility was achieved.

2.3 Nature and morphology of corrosion attack

The nature of corroded products that emerged on the surface of the specimens was analyzed using Energy-dispersive X-ray spectroscopy (EDX) (Make: Oxford Instruments; Model: Inca mics, Sl. No.: 01736). Different corrosion morphologies, observed on the surfaces of the corroded specimens immersed in two different solutions, were examined using both optical and scanning electron microscope (SEM) (Make: JEOL Ltd., Japan; Model: LSM-6360).

3 Results and discussions

The corrosion behavior of modified ferritic stainless steel welded joints prepared under spray (S) and short-circuit (SC)

modes of metal transfer using two different ASS filler metals, such as AISI 308L and AISI 316L, was studied. The main point of interest is to independently determine the corrosion resistance of two different zones in the welded joint, i.e., weld zone and HTHAZ, by means of the anodic polarization technique through linear sweep voltammetry. Since corrosion property is influenced by microstructural heterogeneity of the weld metal and HAZ, the formations of different microstructural constituents in the weldments deduced from different modes of metal transfer using two austenitic filler wires is discussed first followed by the corrosion behavior in terms of microstructural aspect.

3.1 Evolution of weld microstructure

Optical micrograph (Fig. 3) shows that all the welds primarily consist of three phases, i.e., ferrite (δ), austenite (γ), and martensite (α'). However, there are some noticeable variations in between the micrographs of 308L and 316L welds. In the micrographs of 308L welds (SC1 and S1), austenite developed as dark, whereas ferrite remained unaffected (Fig. 3a). Because, austenite in the structure was leaner in chromium owing to partitioning, and it became anodic with respect to ferrite which was richer in chromium and remain passivated during the etching process. Thus, austenite revealed as a thin layer of grain boundary austenite (GBA) or Widmanstätten austenite (WA). On the other hand, Fig. 3b shows more complex microstructures of 316L welds (SC2 and S2). The area represented by the micrographs (Fig. 3b) had undergone a growth of GBA in the interfaces between δ -ferrite grains and a small portion of intragranular austenite (IGA) within the δ -ferrite grains. From the micrographs, it is clear that all the microstructures have primary ferrite and GBA at room temperature. This GBA was also observed from the bright field TEM micrographs of different welds as shown in Fig. 4a, b. Further, TEM micrographs of welds (Fig. 4c, d) revealed the formation of ϵ and α' - martensite.

The variation in weld microstructure can be explained well by the primary solidification modes (PSM) of the respective welds. Depending on the $\text{Cr}_{\text{eq}}/\text{Ni}_{\text{eq}}$ ratio (Table 4) which was derived from the dilution, in the present study, the solidification modes of dissimilar welds could be divided into the following two categories [30–32]:

FA mode: $L \rightarrow L + \delta \rightarrow L + \delta + \gamma \rightarrow \gamma + \delta \rightarrow \gamma$
: 1.48 < $\text{Cr}_{\text{eq}}/\text{Ni}_{\text{eq}}$ < 1.95

FA mode: $L \rightarrow L + \delta \rightarrow \delta \rightarrow \gamma$: $\text{Cr}_{\text{eq}}/\text{Ni}_{\text{eq}}$ > 1.95

It is clearly elucidated from Table 4 that 316L welds (SC2 and S2) having $\text{Cr}_{\text{eq}}/\text{Ni}_{\text{eq}}$ ratio lower than 1.95 solidified as FA mode of solidification, i.e., the precipitation of primary

Fig. 3 Optical micrographs of different welds prepared by **a** 308L and **b** 316L; filler wire under two modes of metal transfer shows various austenite morphologies such as GBA, WA, and IGA in the ferrite matrix

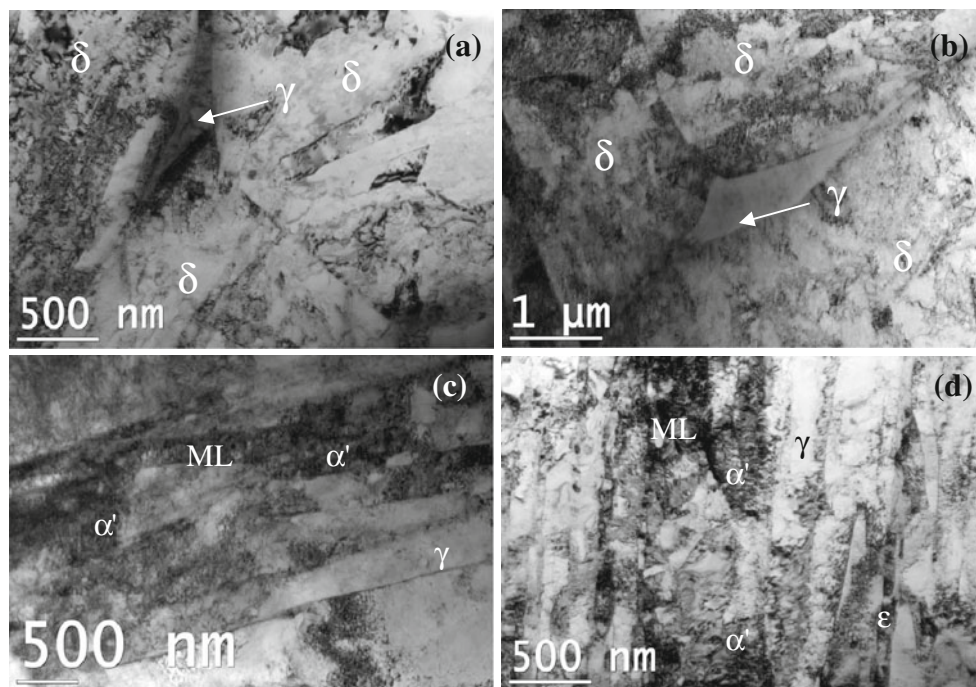
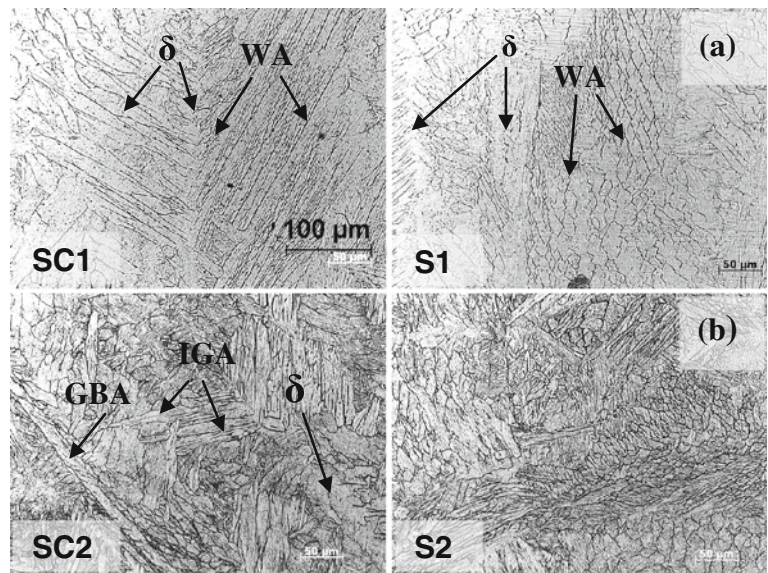


Fig. 4 Bright field TEM micrographs of welds **a** S1 and **b** SC2 shows GBA at the junction of three ferrite grains, **c** S1 and **d** SC2 reveals different forms of martensite

ferrite plus three phase reaction (ferrite, austenite, and liquid) at the terminal solidification stage, and $\delta \rightarrow \gamma$ continuing below the solidus line [33]. Hence, the final microstructure should consist of vermicular δ as a primary phase within the dendritic arms enveloped by the GBA, IGA, and WA [34]. However, 308L welds (SC1 and S1) having Cr_{eq}/Ni_{eq} ratio higher than 1.95 solidified as F mode of solidification. This results in the complete formation of ferrite which may partially transform into austenite during cooling and ultimately leads to the formation of the Widmanstatten

structure [34]. These two solidification modes of welds can also be justified by pseudo-binary phase diagram [35] as presented in Fig. 5, where 316L welds are very close to the γ -solvus line, which clearly indicates the complex FA mode of solidification. The complexity of the 316L weld structure arises from the fact that, after a certain amount of primary solidification as ferrite, austenite precipitation occurs through a peritectic/eutectic reaction ($L + \delta \rightarrow L + \delta + \gamma$). This changes the direction of micro-segregations. Moreover, the subsequent solid-state transformation of $\delta \rightarrow \gamma$ causes

additional partitioning, altering the existing concentration profiles [36]. The unaffected skeletal structure located in dendrite cores is ferrite. On the other hand, 308L welds start to solidify from the right side of the three phase ($L + \delta + \gamma$) zone and remain into the two phase ($\delta + \gamma$) solidification region leading ultimately to primary ferrite and WA formation in final microstructures. Presence of primary ferrite in the weld microstructure can also be supported by the X-ray diffraction patterns as shown in Fig. 6 which reveals major peak intensities of ferrite (bcc), whereas austenite (fcc) phase does not differ significantly, indicating primary ferrite solidification. Therefore, primary solidification processes of welds are exclusively dependent upon the composition of welds in terms of Cr_{eq}/Ni_{eq} ratios

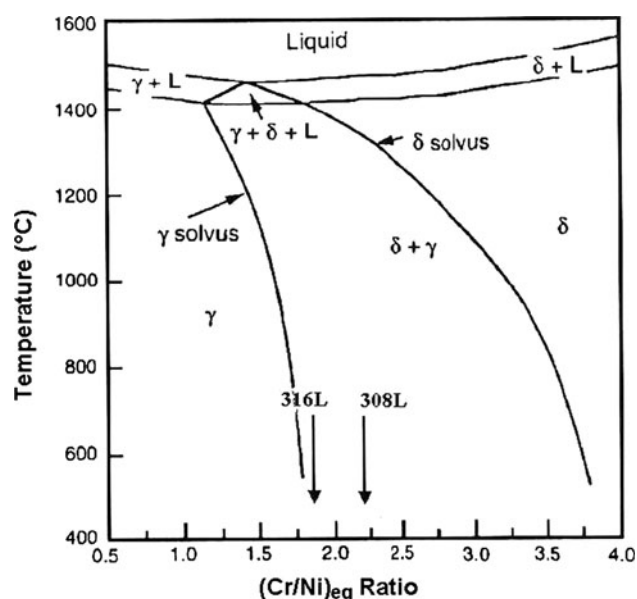
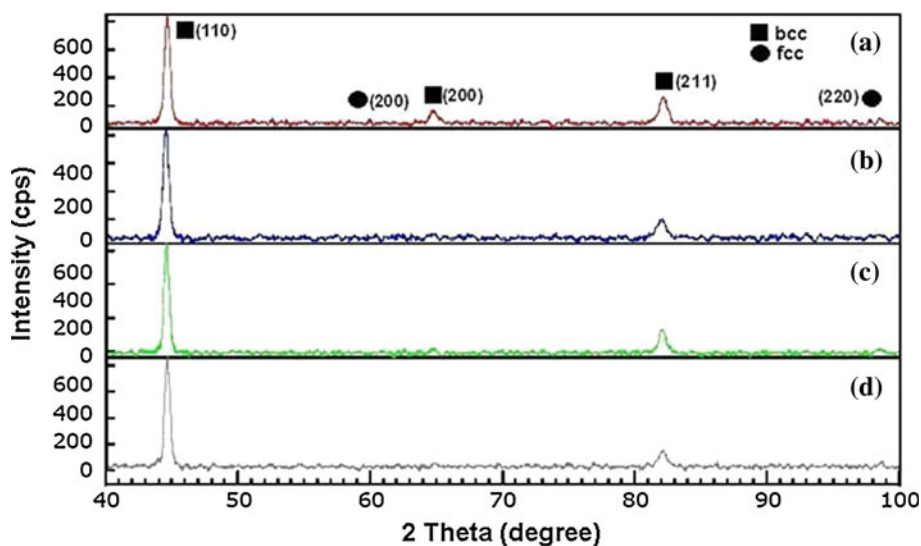


Fig. 5 Pseudo-binary phase diagram for the prediction of equilibrium weld microstructure prepared by two ASS filler metals

Fig. 6 X-ray diffraction pattern collected from different welds of (a) S1; (b) S2; (c) SC1; and (d) SC2 reveals the variable amount of ferrite



irrespective of modes of metal transfer used, although mode of metal transfer has a significant role on controlling the amount of austenite formed at δ -ferrite grain boundaries during the solidification process. Since the solid-state transformation of ferrite into austenite during cooling is nucleation- and growth-controlled, it is postulated that the faster cooling rate experienced by the weld metal at lower heat input, i.e., short-circuit mode (SC1 and SC2) may suppress the $\delta \rightarrow \gamma$ transformation. As the heat input increases, the cooling rate is reduced, i.e., spray mode (S1 and S2) operates and more austenite forms at δ -ferrite grain boundaries which are the preferential location for the nucleation of austenite. The austenite formed at grain boundaries of welds was metastable depending upon their respective Cr_{eq}/Ni_{eq} ratio and tends to transform into lath martensite (denoted as α') [26]. According to Mukherjee et al. [26], the most favored path of solid-state transformation is $\gamma \rightarrow \epsilon \rightarrow \alpha'$, where, ϵ is hcp form of martensite and acts as a precursor to the formation of α' martensite. Their results also appreciably reveal that the S-mode produces more amount of lath martensite than SC-mode for a given filler metal. Therefore, in this study, after complete solidification and transformation, weld microstructure should contain primary ferrite, austenite, and some amount of lath martensite at room temperature.

3.2 Evolution of HTHAZ microstructure

The typical high temperature HAZ (HTHAZ) microstructures of different modes of metal transfer as shown in Fig. 7 revealed ferrite with some martensite. The HTHAZ adjacent to the fusion line represents base metal heated above the A_3 temperature during the weld thermal cycle, and is characterized by δ -ferrite grains surrounded by grain boundary martensite. Unlike weld metal, despite the partial

solid-state phase transformation in HTHAZ from ferrite to austenite on cooling, the HTHAZ is characterized by the coarse grain. Again, Fig. 7 also shows that spray mode attributes relatively higher amount of martensite than short-circuit mode irrespective of the filler wire used. Even the so called higher amount of martensite in S-mode is so low that it is unable to control the grain coarsening in HTHAZ. TEM micrographs of HTHAZ, as shown in Fig. 8, revealed greater dilution of dislocation and presence of martensite. Again, the martensite laths that formed in the HTHAZ are in a premature stage. A number of dislocation lines,

distributed from the boundary to the interior of the ferrite grain in HTHAZ were also observed. This indicated that distributed dislocations did not favor the formation of lath martensite [26]. It is a fact that dislocation pile-up acts rather as a precursor to the martensite formation. These dislocation lines are probably the result of local deformation caused by the residual stress [37] during the weld thermal cycles. Interestingly, HTHAZ in SC-mode having lower martensite than that of S-mode shows finer grains (Fig. 7). This result clearly indicates that the size of the grains is controlled by the cooling rate instead of the

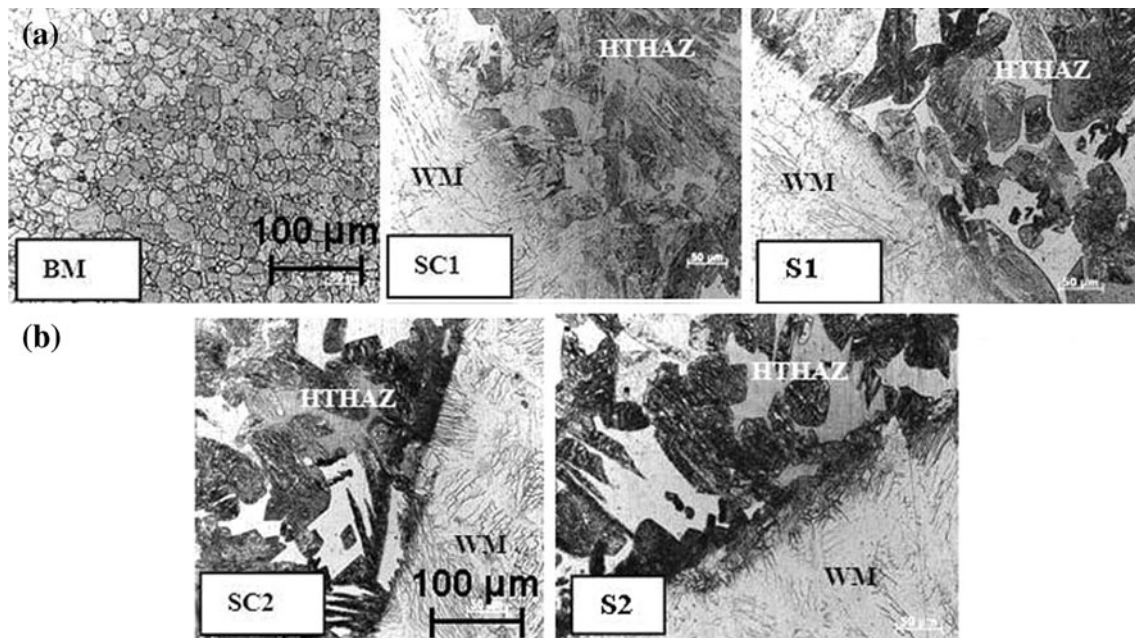
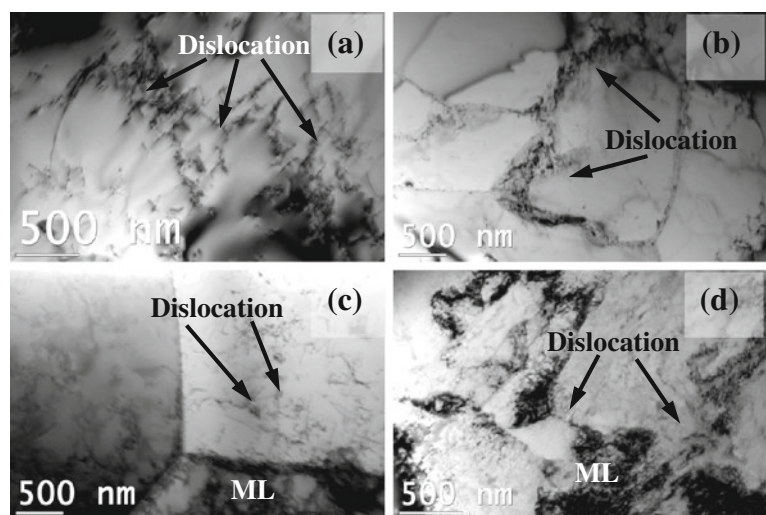


Fig. 7 Optical micrographs of **a** BM along with HTHAZ microstructure of SC1 and S1 and **b** HTHAZ microstructure of SC2 and S2. Micrographs reveal grain coarsening of HTHAZ compared to the BM

Fig. 8 Bright field TEM micrographs of HTHAZ **a** SC1, **b** SC2, **c** S1, and **d** S2 show scattered dislocations and less amount of lath martensite



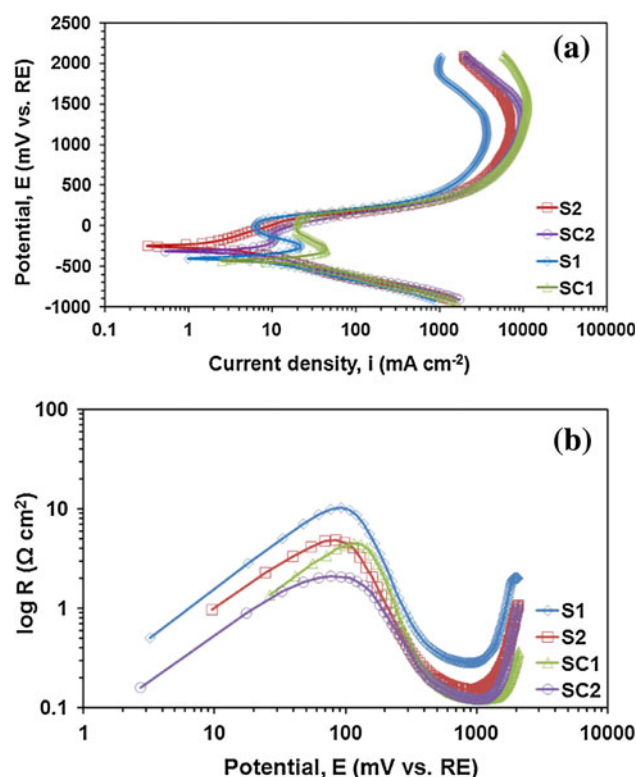


Fig. 9 **a** Potential versus current density curves and **b** resistance versus potential curves of welds after polarization test in 2 M H₂SO₄ solution

martensite content. Thus, spray mode having higher heat input (slower cooling rate) exerted maximum grain growth (coarser grain) in HTHAZ.

3.3 Electrochemical behavior of dissimilar welds in 2 M H₂SO₄ solution

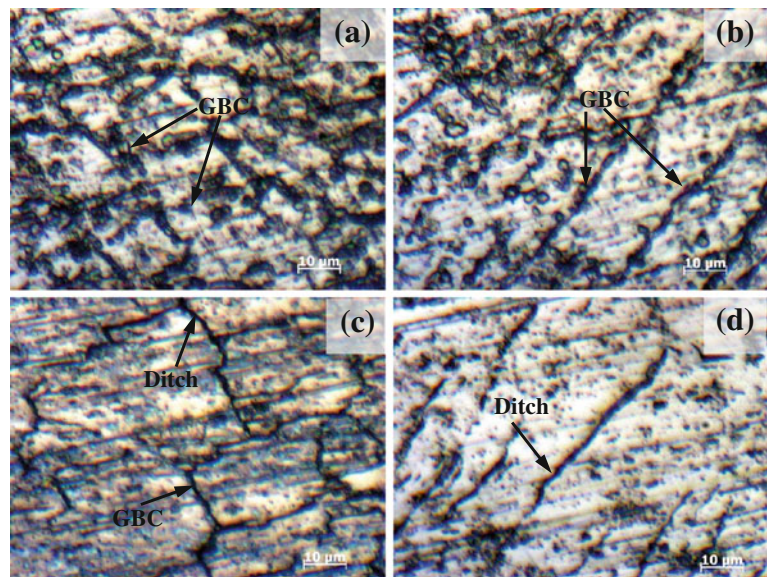
In order to assess the influence of mode of metal transfer and composition on the grain boundary corrosion (GBC) resistance of the welds, anodic polarization measurements

by means of linear sweep voltammetry were performed in 2 M H₂SO₄ solution (Fig. 9). Figure 9a exhibits the polarization curves of the welds in acid medium (containing SO₄²⁻ ions). The anodic peak shifted toward higher current densities for the welds of S1 and SC1 as compared to those of S2 and SC2. Again, between the S1 and SC1, anodic peak further shifted toward higher current density for SC1. Similar results were observed for S2 and SC2. Moreover, the weld metal S2 showed a continuous decrease in the current density as the potential decreased and almost no re-activation; whereas SC2 showed almost similar behavior except a slight re-activation compared with the other two welds (i.e., S1 and SC1). Both S1 and SC1 exhibited clear re-activation. Furthermore, for S2 and SC2, corrosion potential (E_{corr}) shifted toward more noble values compared to the other two welds (S1 and SC1). On the other hand, welds prepared under spray mode had more noble E_{corr} values than welds prepared under short-circuit mode for a given filler metal. The resistance versus potential curves of all the welds at anodic polarization (positive potential) side are plotted in Fig. 9b. The resistance of the curves were calculated on the basis of Ohm's law. Figure 9b clearly illustrates how the resistance near and after the re-activation potential varies with increase in positive potential. The increase in resistance for all weld specimens was noted till a stable corrosion took place. All the curves then decreased until a certain potential was achieved, indicating constant grain boundary corrosion. After a certain level of corrosion, probably re-passivation process started at the corrosion sites, which again increased the resistance with the increasing potential. Furthermore, the resistance of the welds near re-activation potential behaved in a different manner as against that observed near the E_{corr} . In the re-activation region, 308L welds (S1 and SC1) had higher resistance against corrosion compared with the 316L welds (i.e., S2 and SC2). However, the resistivity of different welds near the E_{corr} region had a contrasting nature in comparison to the re-activation

Table 5 Corrosion data of welds after polarization test in 2 M H₂SO₄ and 1 M NaCl

Weld specimens	E_{corr} (mV versus RE)	i_{corr} (mA cm ⁻²)	E_{pit} (mV versus RE)	R _p (ohm)	Corrosion rate (mm year ⁻¹)	PREN
Corrosion data of welds in 2 M H ₂ SO ₄						
SC1	-401	7.18	—	8.45	168.70	—
S1	-383	3.36	—	10.6	86.50	—
SC2	-325	2.60	—	22.7	65.50	—
S2	-253	1.45	—	108.2	34.01	—
Corrosion data of welds in 1 M NaCl						
S1	-345	2.07×10^{-3}	236	$3.05 \times 10^{+3}$	4.86×10^{-2}	16.48
SC1	-323	9.52×10^{-4}	249	$3.21 \times 10^{+3}$	2.23×10^{-2}	16.73
S2	-313	4.76×10^{-4}	258	$1.058 \times 10^{+4}$	1.11×10^{-2}	20.65
SC2	-296	2.73×10^{-4}	298	$1.248 \times 10^{+4}$	6.40×10^{-3}	21.20

Fig. 10 Microstructures of weld zones **a** SC1, **b** S1, **c** SC2, **d** S2; after polarization test in 2 M H₂SO₄ solution



region. The variation in resistance from E_{corr} to re-activation potential was correlated with the passive film resistance with or without the presence of Mo in the welds later in this section, although, it is important to be mentioned here that overall resistivity of the bulk materials did not differ with the local resistance variation. The results of polarization studies at corrosion potential are presented in Table 5, which comprise E_{corr} , i_{corr} , R_p , and corrosion rate values depending on filler wire composition and mode of metal transfer. It could also be observed from Table 5, how the corrosion rate varied among the welds. In general, the welds produced under SC-mode had higher corrosion rate than those produced under S-mode of metal transfer.

With the aim to complete the grain boundary corrosion study, surface morphologies of the welded specimens were studied after the electrochemical test by optical microscopy. The observation of the surface morphology of the weld samples after the electrochemical tests disclosed the following (Fig. 10): SC1 and SC2 facilitated generation of higher amounts of GBC compared with S1 and S2, probably associated with the Cr depletion mechanism along the δ/δ or δ/γ -grain boundaries. Between the two filler metals, 308L welds revealed the highest amount of GBC for the same mode of metal transfer, whereas the corrosion attack was notably reduced for 316L welds. Figure 10 also shows that the electrode surfaces dissolve generally in the solution. However, the corrosion attack mainly concentrated in or near the grain boundary regions, which is the clear evidence of GBC. In addition, surface morphologies of the welds also indicate the ditch type structure which is the evidence of grain boundary corrosion (GBC) [38].

In order to examine the surface morphology and alloy segregation in greater detail, a detailed SEM study of the corrosion sites of the tested materials was carried out.

Figure 11 shows an SEM analysis of SC1, S1, and SC2, after the electrochemical polarization test, which revealed GBC on δ/δ -grain boundaries and little transgranular corrosion (TGC) on the δ/γ interface. TGC occurred only in weld metal SC1 along with GBC, while in other welds, mainly GBC plays a dominant role to determine the corrosion behavior. Due to simultaneous occurrence of TGC and GBC, weld metal SC1 had the highest corrosion susceptibility among all the other welds as revealed in Table 5. Furthermore, SEM micrographs (Fig. 11) also disclose that the occurrence of GBC was discontinuous along the grain boundary, i.e., some portion of the grain boundary was attacked by the acidic media and some portions were left untouched. The EDX area scan (Fig. 12) revealed that the segregation of Cr and Ni varied for all the welds. Due to the similar trend between the welds, two extreme conditions, i.e., S1 and SC2 were summarized in Fig. 12. From Fig. 12 it is clear that, Cr-depleted and Ni-enriched zones had been formed near the grain boundary in the welds, whereas, Cr content at the interior of the grain was high enough to prevent the corrosion by forming comparatively stronger passive film during the electrochemical test. Therefore, due to weak passive film formation, corrosion attack should be localized near the grain boundary regions [38].

The grain boundary corrosion resistance of the welds can be explained in the following two ways: the Cr depletion mechanism along the grain boundaries and the PSM. The Cr depletion along the grain boundary is mainly dependent upon the alloy segregation, particularly Cr, Nb, and Ni, around the carbides. However, the presence of GBA can significantly alter the alloy segregation by absorbing free carbon rejected from ferrite during solidification. Ferrite–ferrite grain boundaries are the most

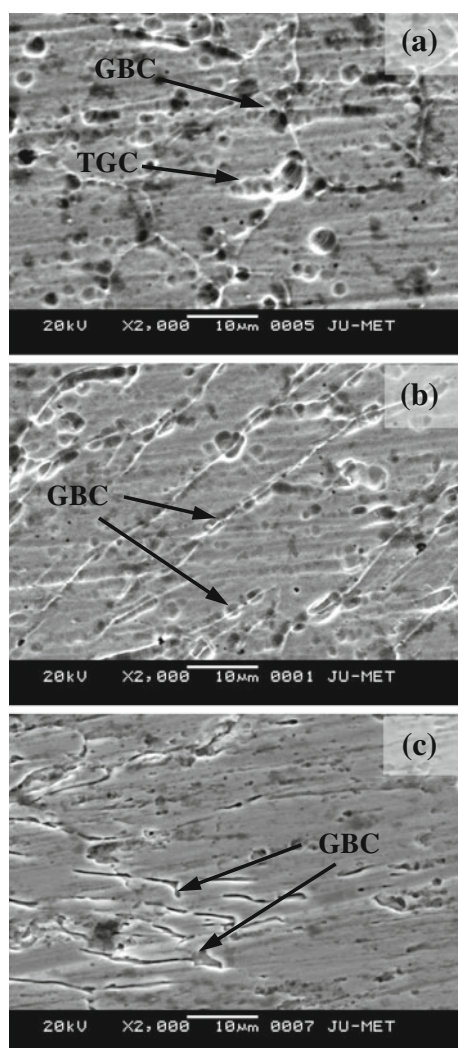


Fig. 11 SEM micrographs of welds **a** SC1, **b** S1, and **c** SC2 after polarization test in 2 M H₂SO₄

preferable sites for Cr segregation and carbide formation [18] due to the negligible presence of austenite as shown schematically in Fig. 13a. Therefore, Cr-depleted region is formed around the grain boundary carbide precipitates. However, formation of austenite along the grain boundary reduces the tendency to form carbide precipitation and the degree of the Cr depletion decreases [39]. Austenite formation along the grain boundary and its quantity are undoubtedly dependent upon the modes of metal transfer. The higher amount of GBA of the welds prepared under S-mode are attributed to the slower cooling rate [26] as compared with the welds prepared under SC-mode for a given filler metal. Higher amount of GBA formation in S-mode absorbs more carbon, and hence, reduces the Cr-depleted regions because of a longer amount of available time for back diffusion of Cr into the depleted zone, which ultimately increases the corrosion resistance of welds under S-mode as schematically represented in Fig. 13b. EDX

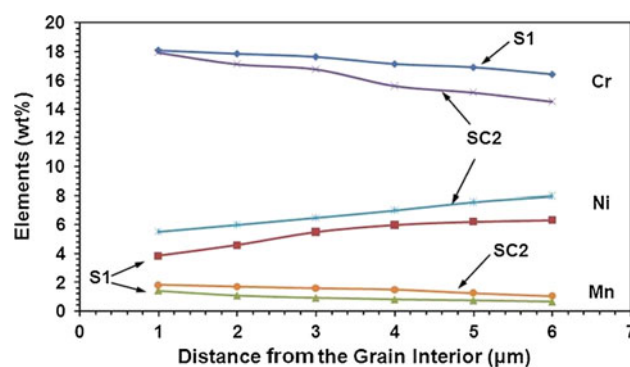


Fig. 12 EDX analysis of welds S1 and SC2 shows the Cr, Ni, and Mn segregation from grain interior to the grain boundary. The diagram suggests that the Cr-depleted and Ni-enriched zones had been formed near the grain boundary and varies with the mode of metal transfer such as SC-mode had higher Cr-depleted zones than the S-mode

small area scan of different welds (Fig. 12) also reveals lower Cr depletion near grain boundary of S-mode as compared to SC-mode, which ultimately suggests that the corrosion resistance is improved (Table 5) to a certain extent and thus the E_{corr} is shifted to a nobler value (Fig. 9a) with S-mode of metal transfer. Carbides are more prone to precipitate in the welds produced under SC-mode with high ferrite content, and thus lesser austenite formation produces Cr-depleted region around them, inducing preferential sites for corrosion [40, 41] as schematically shown in Fig. 13c. Therefore, the occurrence of GBA explains well the discontinuous corrosion behavior (Fig. 11) along the grain boundary of the welds. Besides the δ/δ grain boundaries, Cr-depleted regions can also be found along the δ/γ interface boundaries as shown schematically in Fig. 13d. Along the interface, different alloying elements such as Cr, C, Ni etc. that were rejected from ferrite try to diffuse and dissolve in the austenite side even at the lower temperature. As the temperature decreases, the diffusion becomes so slow that some carbon remains in the interface along with Cr and Ni creating intragranular carbide precipitations. Therefore, along the ferrite–austenite interface boundary, Cr-depleted zones may be observed around the precipitates, which, in turn, influences the TGC of the welds. Modes of metal transfer also influence the interface mechanism by reducing austenite and increasing ferrite in the welds of SC-mode compared to that of S-mode. Higher ferrite content creates more depleted zones and thus, increases the tendency of TGC in SC1 (Fig. 11a), although, unlike SC1, SC2 does not reveal any TGC, and this phenomenon can be explained with the help of primary solidification mode (PSM) between welds.

The PSM influences the corrosion resistance of the welds by producing more GBA in the weld microstructure. In the present study, 316L welds (SC2 and S2) were solidified in FA mode depending upon their $\text{Cr}_{\text{eq}}/\text{Ni}_{\text{eq}}$

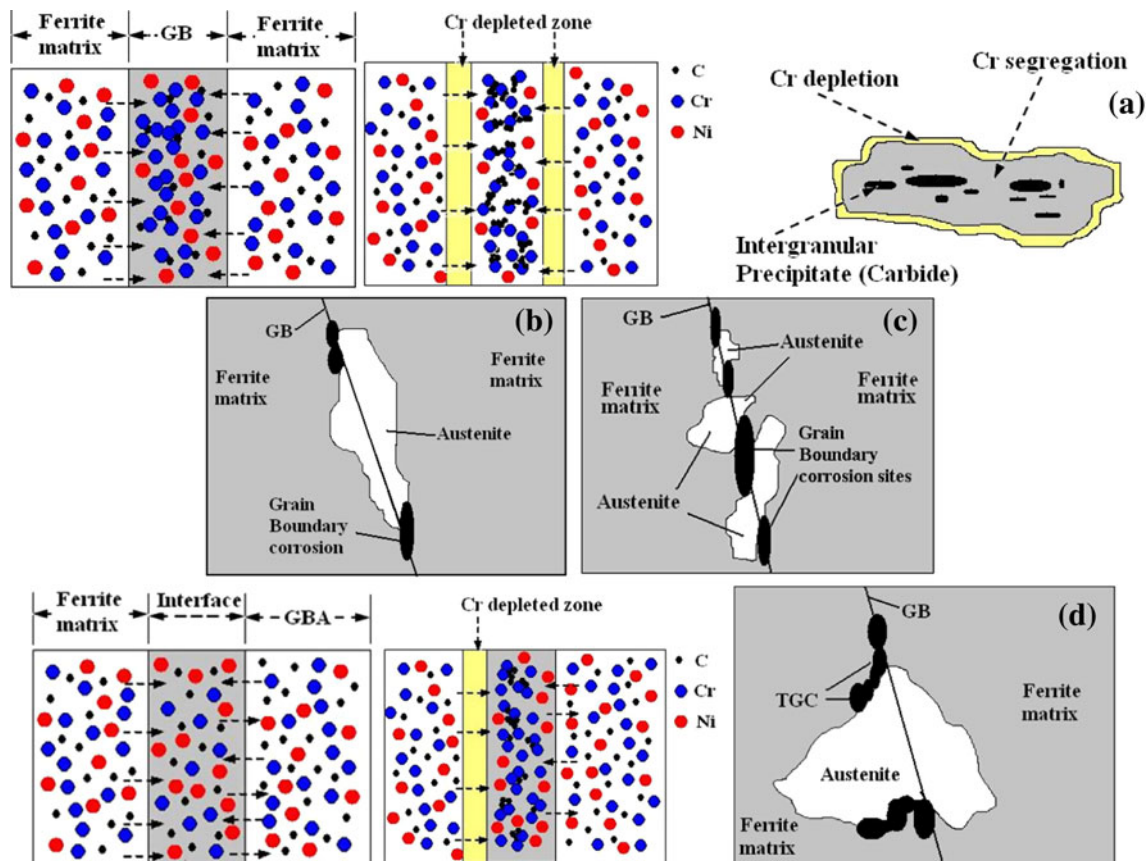


Fig. 13 Schematic illustrations of corrosion mechanisms **a** Cr-depleted regions formed along the δ/δ grain boundary, **b** formation of higher amount of GBA in S mode which reduces the GBC sites,

c lower GBA formation in SC mode which enhances the GBC sites and **d** TGC explained by the Cr-depleted regions formed along the δ/γ -interface boundary

ratios, where more amount of GBA had been formed (Fig. 3b) at high temperature, which absorbed the free carbon rejected from the ferrite and experienced less grain boundary and transgranular corrosion (Fig. 10c, d) [42]. In 308L welds (SC1 and S1), although little WA was formed along the grain boundaries (Fig. 3a) due to F mode of solidification, the grain boundaries, after solidification, approach the composition of the Ni-enriched and Cr-depleted regions due to the presence of higher amount of ferrite in the matrix. This causes higher segregation of Cr and Ni, and at the same time, absorption of rejected carbon from ferrite is very low in WA. Both these phenomena were unable to resist GBC and TGC (Fig. 11a, b) in 308L welds.

In addition, the variation in the corrosion resistance during re-activation potential (Fig. 9b) was correlated with the passive film resistance by means of the presence of molybdenum (Mo) in the passive film. Mo-containing welds (i.e., S2 and SC2) have lower resistance during the re-activation process as compared with the non-Mo species (i.e., S1 and SC1). The influence of molybdenum on resistance can be explained well by an excellent study

made by Bojinov et al. [14] using mixed-conduction model (MCM). According to their work, the MCM predicts that oxidative or reductive changes of the stoichiometry mainly in the first layers of the film close to its interface can lead to defect-induced conductivity of the whole film. As the film thickness at room temperature is very close to the limit of tunneling distance, a sufficient accumulation of defects at the two interfaces leads to the transformation of the passive layer to a good electronic and ionic conductor. This in turn may lead to the release of soluble products both during the re-activation and transpassive dissolution, thus decreasing the resistance of the film both in the re-activation and transpassive regions. In the present study, the presence of Mo in passive film may increase the electronic conductivity of the films formed on the respective welds. This is most likely connected with an increase of the non-stoichiometry of the film in the presence of Mo. During the re-activation of the Mo-containing welds (i.e., S2 and SC2), soluble products should release at a higher rate than those during the re-activation of the non Mo-containing welds (i.e., S1 and SC1). In addition, Mo had an accelerating effect on the dissolution during re-activation if the welds do not contain

a sufficient amount of Cr and by extension $\text{Cr}_{\text{eq}}/\text{Ni}_{\text{eq}}$ ratios of the respective welds. This is an important observation while considering the role of relative amounts of alloying elements [14] in the prevention of GBC. Consequently, a higher dissolution during re-activation and lower $\text{Cr}_{\text{eq}}/\text{Ni}_{\text{eq}}$ ratio of welds SC2 and S2 generate the prominent ditch [38] type corrosion morphology in the respective welds (Fig. 10c, d). Furthermore, presence of Mo also greatly reduces the current density and increases the resistance of both the active dissolution and the prepassive dissolution regions compared with the non-Mo welds [14], and therefore, explains the higher resistivity of the 316L welds during E_{corr} (Fig. 9a). Hence, it can be concluded that the presence of Mo in the passive film has a twofold effect on the resistance: at first, it increases the resistance up to re-activation region and then decreases, although the bulk resistance of the welds are mainly governed by the first process as depicted in Table 5.

3.4 Electrochemical behavior of dissimilar welds in 1 M NaCl solution

In order to assess the influence of mode of metal transfer and composition on the pitting corrosion resistance of the FSS welds, anodic polarization measurements by means of linear sweep voltammetry were performed in 1 M NaCl solution (Fig. 14). The corrosion potential (E_{corr}) of 316L welds (SC2 and S2) shifted slightly to more nobler values compared with the 308L welds (SC1 and S1) and increased the pitting corrosion resistance, determined by the pitting potential (E_{pit}) as shown in Fig. 14a. The resistance versus potential curves for all the welds are shown in Fig. 14b. It clearly represents how the bulk resistance varied with increase in positive potential. The increase in resistance for all the welds was noted until a stable pitting corrosion took place, after which the curve decreases depicting the stable pit growth. The results of polarization studies are collected in Table 5, which comprise E_{corr} , E_{pit} , R_p , and corrosion rate values and also the different ranges defined between these potentials, depending on filler wire compositions and mode of metal transfer. For similar filler metal (i.e., 308L), S-mode of metal transfer shifted E_{corr} and E_{pit} values from -323 to -345 mV versus RE, and from 249 to 236 mV versus RE, respectively, compared to SC-mode. A similar observation can be found for the other filler metal (i.e., 316L) as shown in Table 5. Conversely, for a given mode of metal transfer, these potentials are displaced toward less nobler values from 316L welds to 308L welds. Table 5 also reveals that resistance to pitting corrosion (R_p) improved with SC1 and SC2 compared to S1 and S2, which was clearly reflected in the corrosion rate of the welds.

With the aim to complete the pitting corrosion study, surface morphologies of the welded specimens were

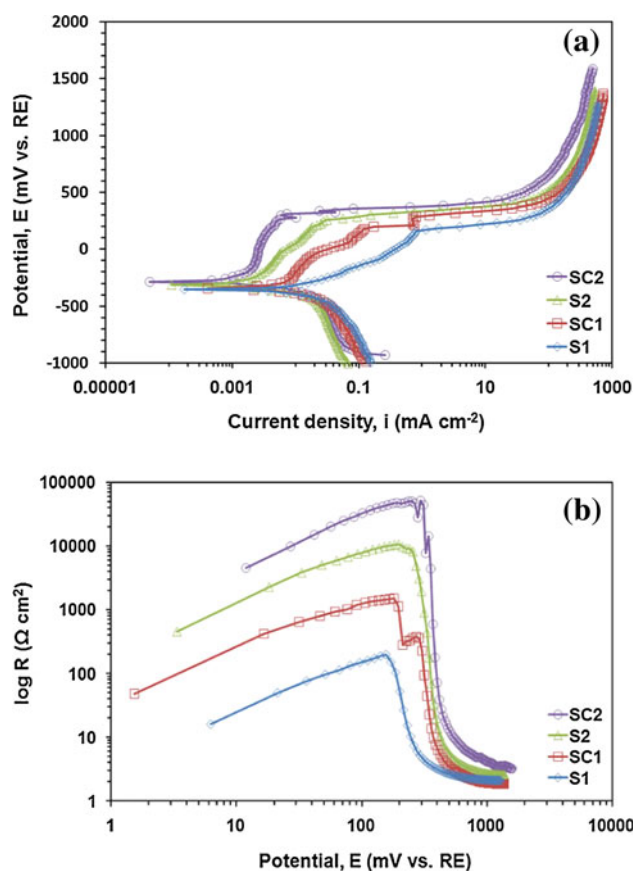


Fig. 14 **a** Potential versus current density curves and **b** resistance versus potential curves of welds after polarization test in 1 M NaCl solution

studied after the electrochemical test by optical microscopy. The observation of the surface morphology after the electrochemical tests disclosed the following (Fig. 15): S1 and S2 facilitated generation of a larger number of pits compared to SC1 and SC2, probably associated with the formation of sulfide and/or oxide inclusions. Certainly, 308L welds revealed the highest amount of pits for the same mode of metal transfer, whereas for 316L welds, pitting corrosion susceptibility was notably reduced.

In order to examine the effect of inclusions and passive film breakdown on the corrosion attack, a detailed SEM study of the pitting initiation of the tested materials was carried out. Figure 16 shows SEM analysis of S2 and S1 around an inclusion, which reveals that, after the electrochemical polarization test, the inclusion was partly dissolved. The EDX analysis in Fig. 16a shows relatively large peaks of Mn and S in a proportion close to the stoichiometric MnS. Figure 16b reflects the concentration profile of Fe, Cr, O around a pit of the specimen S1, which clearly denotes the presence of oxides. Furthermore, Fig. 17 discloses SEM analysis of the specimen S2 polarized under the same conditions. Several inclusions were

Fig. 15 Microstructures of weld zones **a** SC1, **b** S1, **c** SC2, **d** S2; after polarization test in 1 M NaCl solution

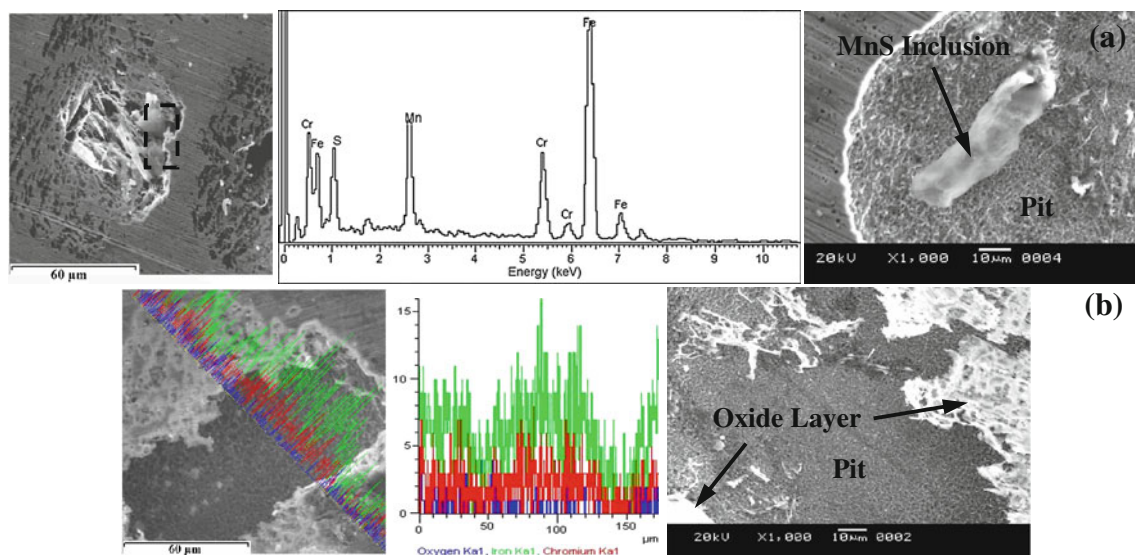
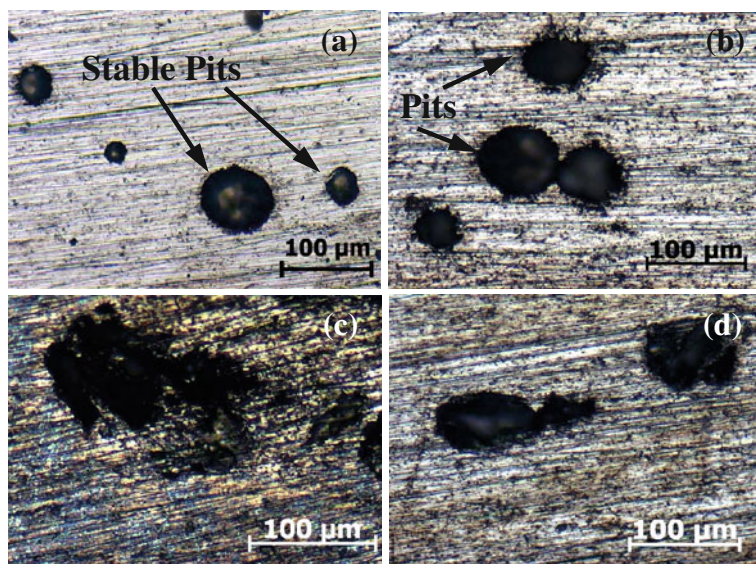


Fig. 16 SEM and EDX analysis reveals the **a** peak of Mn and S indicating the presence of MnS inclusion in the weld of S2 and **b** concentrations of Fe, Cr, O around a pit illustrates the presence of oxides in the weld of S1; after polarization test in 1 M NaCl solution

found to be at their dissolution stage and partially covered with some corrosion products which contained high amounts of Mo and O along with Fe and Cr, detected by X-ray mapping and EDX analysis.

The pitting corrosion resistance of welds under different modes of metal transfer using two austenitic filler metals (i.e., 308L and 316L) can be explained in the following two ways: pitting corrosion resistance of the bulk welds and the localized pitting corrosion mechanism related to the formation of inclusions. The pitting corrosion resistance of the bulk welds is mainly influenced by the alloying elements, although in the welds, the main alloying elements, i.e., chromium, molybdenum, nickel, and nitrogen are not

evenly distributed in ferrite and austenite. Chromium and molybdenum should enrich in ferrite, whereas nickel and nitrogen are concentrated in austenite. From the microstructural evaluation, it was confirmed that the primary solidification modes of all welds are ferrite. However, the formation of austenite and its concentration along the grain boundaries strictly depend upon the Cr_{eq}/Ni_{eq} ratio and modes of metal transfer. Mode of metal transfer significantly alters the dilution process and thus, varying the Cr_{eq}/Ni_{eq} ratio of the welds. The influence of the alloying elements on pitting corrosion resistance can be simplified by pitting resistance equivalent number (PREN), given by $PREN = \%Cr + 3.3 \%Mo + 20 \%N$ [43]. The variation

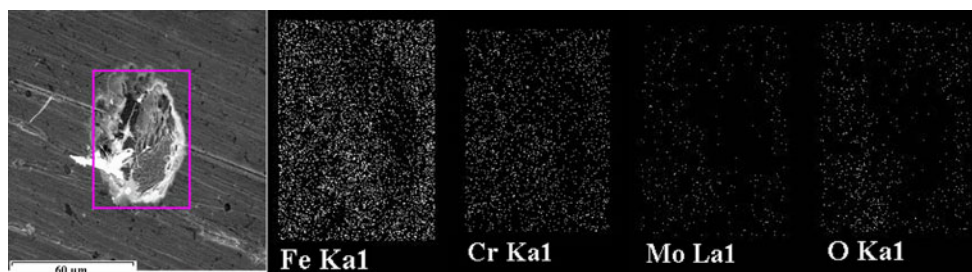


Fig. 17 Selected area elemental mapping by EDX shows the concentrations of Fe, Cr, Mo, O around a pit in the weld of S2

in $\text{Cr}_{\text{eq}}/\text{Ni}_{\text{eq}}$ ratio and mode of metal transfer as well significantly altered the PREN values of different phases. The PREN values of welds are calculated and listed in Table 5. The PREN values of different welds can be presented in increasing order as follows: S1 \rightarrow SC1 \rightarrow S2 \rightarrow SC2.

The relationship between PREN and E_{pit} with the $\text{Cr}_{\text{eq}}/\text{Ni}_{\text{eq}}$ ratio is exhibited in Fig. 18. The result shows that as the $\text{Cr}_{\text{eq}}/\text{Ni}_{\text{eq}}$ ratio increases, PREN and E_{pit} decreases. A higher $\text{Cr}_{\text{eq}}/\text{Ni}_{\text{eq}}$ ratio increases the stability of ferrite, due to favorable F-mode solidification path, in the bulk weld metal. It was previously reported that ferrite phase is less resistant than austenite phase and pitting always occurred in ferrite phase [44]. For a given filler metal, S-mode had higher $\text{Cr}_{\text{eq}}/\text{Ni}_{\text{eq}}$ ratio than SC-mode inducing more ferrite (as δ -ferrite and/or α' -martensite) in the welds, and reducing the PREN value (Fig. 18a), thus declining the pitting corrosion resistance of the whole alloy (Fig. 14b) by shifting the E_{pit} values to less noble potential (Fig. 18b). Therefore, $\text{Cr}_{\text{eq}}/\text{Ni}_{\text{eq}}$ ratios can be taken as an indexing parameter instead of PREN for determining the pitting corrosion resistance of the welds due to involvement of more alloying elements which have both direct and indirect influence on the pitting behavior.

In addition to the $\text{Cr}_{\text{eq}}/\text{Ni}_{\text{eq}}$ ratios, typical presence of some alloying elements (such as Mo, Mn, and S) has a major effect on the pitting corrosion resistance of the welds. It was reported that Mn has a strong affinity to sulfur to form highly stable MnS inclusions and, as a consequence, it usually appears to form these sulfides within weld microstructure [45]. This result is confirmed by SEM examination (Fig. 16) of the specimens and an evident correlation between Mn content and MnS formation is observed. MnS is known as the most common site for pit nucleation, since it can be anodically polarized within the passivity region observed for stainless steels [46]. Under these conditions, MnS inclusions are not stable and tend to dissolve, initiating an attack at the inclusion/matrix interfaces, which results in the generation of cationic species of the alloy elements such as Fe^{2+} , Ni^{2+} , Cr^{3+} , and in particular, Mo^{3+} [45]. Several works have shown that the dissolution of a sulfide inclusion is the initial step before any further pit propagation at the pitting site in chloride-

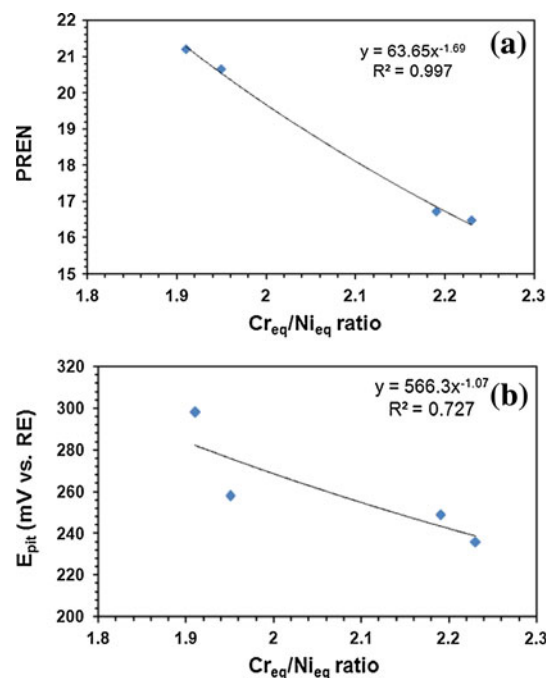


Fig. 18 Correlation between **a** PREN versus $\text{Cr}_{\text{eq}}/\text{Ni}_{\text{eq}}$ ratio and **b** E_{pit} versus $\text{Cr}_{\text{eq}}/\text{Ni}_{\text{eq}}$ ratio; of welds

containing solutions [45, 47]. Thus, Mn content should promote the formation of manganese sulfides and therefore, increase the pitting attack susceptibility of the welds. Although the amount of Mn and S present in the welds are more or less same (Table 4), variation in pitting resistance between the welds can only be explained by other alloying elements present such as Mo which play an important role toward the pitting resistance of the welds [48–50].

Presence of Mo in 316L welds enhances the pitting corrosion resistance in 1 M NaCl, reducing progressively the corrosion rate (Table 5) and shifted both E_{pit} and E_{corr} values to nobler potentials (Fig. 14a). As a result, 308L welds are less resistant to stable pitting. This is consistent with early findings which reported that the pitting resistance of Mo-containing stainless steels is superior to that of non-Mo-containing ones [45, 48]. It is known that Mo may have an effect on more than one step in a pitting event. In the first instance, Mo modifies the passive film rendering it

more stable against breakdown caused by the attack of aggressive Cl^- ions [49] and, in the second instance, the presence of Mo within the alloy significantly improves the repassivation behavior or deactivation of growing pits [50]. In this work, it can be assumed that the alloy was almost free of non-metallic inclusions or its content was low and more or less same over the different welds. Nevertheless, for the welds evaluated here, the presence of MnS inclusions allows revealing different mechanisms of Mo action, supporting an important effect at the stages of metastability and growth of pits. Under the acidic conditions, Mo is quickly dissolved, allowing the formation of a great amount of oxidized species, such as FeMoO_4 [45], which partially or entirely cover the pit wall. As a result, pits at the metastable stage were repassivated and the probability of achieving their stable stage is reduced for the Mo-containing welds (i.e., SC2 and S2) [50] whereas, repassivation was delayed due to slow generation of cationic species of the alloy elements such as Fe^{2+} , Cr^{3+} in non-Mo-containing welds (i.e., SC1 and S1) which leads to stable pit formation on the surface (Fig. 15a, b). Therefore, it can be concluded from the above discussion that, under the same mode of metal transfer, 316L welds (i.e., SC2 and S2) had less pitting tendency compared with the 308L welds.

3.5 Electrochemical behavior of HTHAZ in 2 M H_2SO_4 and 1 M NaCl solutions

Electrochemical behavior of HTHAZ in H_2SO_4 and NaCl is an important criterion of stainless steel welded joints. For this purpose, anodic polarization tests using linear sweep voltammetry method were employed to evaluate the corrosion resistance. Mode of metal transfer has an exclusive effect on the HTHAZ microstructure and alters the corrosion properties. Therefore, only two extreme conditions of mode of metal transfer, i.e., S-mode and SC-mode were depicted in the study. The polarization curves for the specimens with various modes of metal transfer are compared in Fig. 19. The S-mode shifted E_{corr} toward more nobler potentials compared to the SC-mode (Fig. 19a), and hence, improved the corrosion resistance in H_2SO_4 . Pitting corrosion resistance also improved with the S-mode due to nobler E_{pit} value as shown in Fig. 19b. Pitting corrosion polarization curve (Fig. 19b) also depicted a higher passive region of the HTHAZ in SC-mode. In addition, Table 6 listed the summary of E_{corr} , i_{corr} , E_{pit} , R_p , and corrosion rate determined by the polarization test results. Among these, i_{corr} as anodic activation peak current density was almost the same for all the specimens, indicating that the presence of reformed austenite did not show obvious effects on the anodic active dissolution. The E_{corr} values which were in the range of -405 mV (RE) to -420 mV (RE) for H_2SO_4 and in the range of -330 mV (RE) to

-760 mV (RE) for NaCl, increased with higher heat input, i.e., spray mode. Therefore, the test results indicated that the corrosion resistance of the HTHAZ increases with S-mode, suggesting an improved bulk resistance in both the solutions, which was also, reflected in the corrosion rates (Table 6). Similarly, pitting resistance of the HTHAZ, determined by E_{pit} , also improved with the spray mode of metal transfer. However, the variation in pitting corrosion properties between the two modes of metal transfer was very close to each other.

The observation of the surface morphology in optical microscope (Fig. 20) and SEM (Fig. 21) of the HTHAZ specimens after the electrochemical tests disclosed the following: after the electrochemical test in H_2SO_4 , SC-mode showed higher grain boundary attack than that of the S-mode (Fig. 20a). On the other hand, HTHAZ of SC-mode had larger pit size compared to the S-mode revealing stable pit formation and growth (Fig. 21a). Secondly, some oxides (probably a complex Fe–Cr–O type) were formed on the pit wall of HTHAZ under SC-mode and these were absent in the S-mode. This formation of oxides attempted to repassivate the pits and probably increased the passive region of the HTHAZ under SC-mode as shown in Fig. 19b.

Grain boundary attack and pitting corrosion behavior of HTHAZ under different modes of metal transfer, i.e., SC-mode and S-mode can be explained well by the

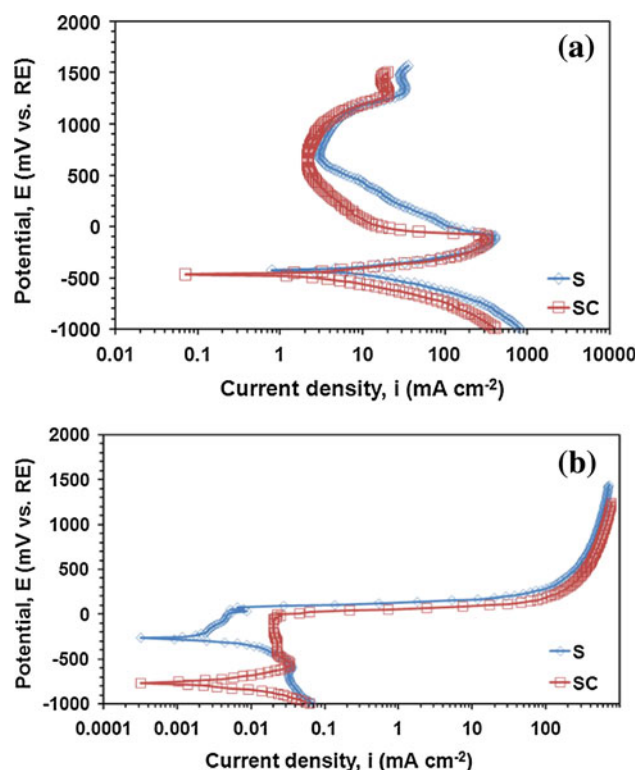
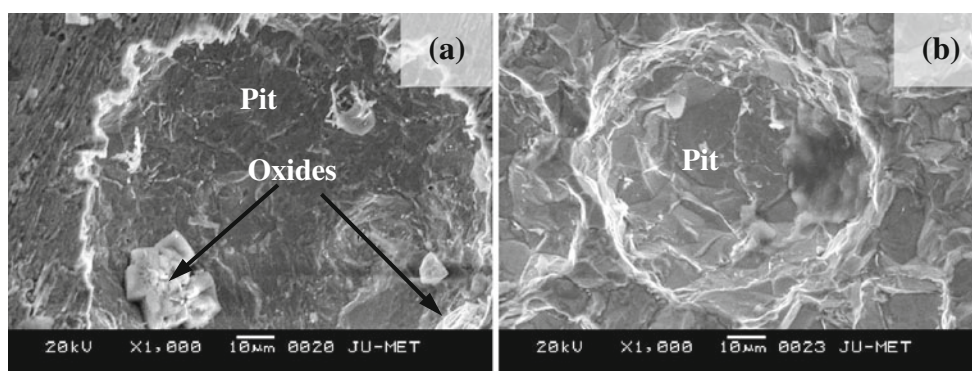
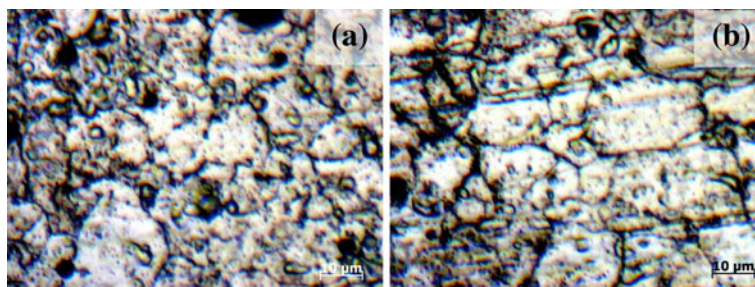


Fig. 19 Polarization curves of HTHAZ under different modes of metal transfer **a** in H_2SO_4 solution and **b** in NaCl solution

Table 6 Corrosion data of HTHAZ after polarization test in 2 M H₂SO₄ and 1 M NaCl

HTHAZ specimen	E_{corr} (mV versus RE)	i_{corr} (mA cm ⁻²)	E_{pit} (mV versus RE)	R_p (ohm)	Corrosion rate (mm year ⁻¹)
Corrosion data of HTHAZ in 2 M H ₂ SO ₄					
S1	-410	4.40	–	19.20	103.2
SC2	-417	4.16	–	11.32	121.3
Corrosion data of HTHAZ in 1 M NaCl					
S2	-324	6.87×10^{-4}	25	$2.76 \times 10^{+4}$	1.61×10^{-2}
SC1	-756	7.90×10^{-4}	19	$2.53 \times 10^{+4}$	1.85×10^{-2}

Fig. 20 Microstructures of HTHAZ under **a** SC2, **b** S1, after polarization test in 2 M H₂SO₄ solution show the localized grain boundary attack**Fig. 21** SEM micrographs of HTHAZ under **a** SC1 and **b** S2 show pit morphology after polarization test in 1 M NaCl solution

sensitization during the weld thermal cycle. Several studies [24, 25] were performed on the contribution of the thermal history to the degree of sensitization in different grades of stainless steel, particularly the influence of mode of metal transfer or heat input and the extent of cooling rate. For FSS, it is established that low heat input such as SC-mode of metal transfer results in very fast cooling rates during the early stages of the weld thermal cycle, therefore, suppressing austenite nucleation at the HTHAZ; as the HAZ cools through the dual-phase ($\alpha + \gamma$) field, it produces practically fully ferritic microstructures. Since the solubility of carbon in ferrite is very low, the phase becomes supersaturated in carbon. This produces extensive carbide precipitation at the ferrite–ferrite grain boundaries and even in the ferrite grains during the cooling cycle (Fig. 13). SC-mode of metal transfer equally prevents back diffusion of chromium to the depleted regions adjacent to the chromium-rich carbides, creating a network of sensitised zones

[24]. As weld heat input increases in S-mode, the cooling rate becomes slower; much more GBA is formed at the δ/δ boundary interfaces (Fig. 13b); and interstitial elements diffuse to and dissolve in the austenite, thus, reducing the amount of interstitial precipitates. If the presence of these boundary interfaces is not covered by GBA, then it would easily lead to the occurrence of grain boundary corrosion [51] due to sensitization, as shown in the Fig. 20. Therefore, HTHAZ under SC-mode produces more grain boundary corrosion compared to the HTHAZ under S-mode. Moreover, the presence of martensite in the HTHAZ (Fig. 8) can also prevent GBC by decreasing the probability of Cr depletion near grain boundaries by absorbing free carbons rejected from the ferrite phase during cooling [24]. At lower temperatures around 800–500 °C, the austenite transforms to martensite and is retained down to room temperature as grain boundary lath martensite (Fig. 8) within a HTHAZ microstructure [24].

The amount of carbon retained in the martensite depends on the mode of metal transfer. Although the amount of martensite (transformed from austenite during cooling) was lesser in quantity, it increased with higher heat input, i.e., spray mode of metal transfer [26], presenting better recovery ability of passive layer or depleted zones around the precipitates. The interstitial precipitates act as a pit initiation site, due to the chromium-depleted regions formed around them, and reduce the pitting resistance of the HTHAZ under SC-mode, which, eventually, increases the stability of the pits and assists the pit growth (Fig. 21a). Therefore, it appears that S-mode of metal transfer is very essential to reduce and/or control sensitization in FSS HTHAZ. This is because these conditions permit healing of chromium-depleted regions around the precipitate by means of desensitization process [25].

4 Conclusions

From the above studies, following conclusions can be drawn:

1. Primary solidification mode (PSM) of the welds were exclusively dependent upon the Cr_{eq}/Ni_{eq} ratios of the respective welds. Cr_{eq}/Ni_{eq} ratio > 1.95 leads to F mode of solidification, and the values below 1.95 lead to FA mode of solidification in the welds.
2. The amount of GBA formation in the welds was dependent upon the mode of metal transfer and the extent of cooling rate. SC-mode of metal transfer or faster cooling rate generate lower amount of GBA in the welds SC1 and SC2, whereas, S-mode or slower cooling rate produce relatively higher amount of austenite along the grain boundary. Some parts of these GBA also transformed into lath martensite during cooling.
3. Heat-affected zone, solely influenced by mode of metal transfer, showed coarser structure compared with the base metal along with some scattered lath martensite formation. As the heat input increased from SC-mode to S-mode, grains became coarser and the scattered lath martensite was unable to restrict the grain coarsening.
4. Grain boundary corrosion (GBC) behavior of welds entirely depends upon the microstructural changes along the grain boundary due to the variation in the mode of metal transfer. Spray mode of metal transfer induced higher GBA formation and thus, decreased the GBC compared to the SC-mode. For a given mode of metal transfer, GBC behavior of welds was also dependent upon the filler wire used. 316L welds (SC2 and S2), in general, decreased the corrosion rate.

However, corrosion rate of 308L weld under S-mode had close proximity with the 316L welds.

5. Pitting corrosion resistance of welds was mainly governed by the following three factors: Cr_{eq}/Ni_{eq} ratio of the welds, the presence of sulfide inclusions, and the formation of Mo oxides around the pits. S-mode of metal transfer comprising more ferrite, due to higher Cr_{eq}/Ni_{eq} ratio, increased the pitting susceptibility compared to the SC-mode of metal transfer. The pits were mainly observed around the sulfide inclusions due to the localized passive film break down. For a given mode of metal transfer, 316L welds had better pitting corrosion resistance than 308L welds. The presence of Mo in the welds of 316L creates the stable Mo oxides around the pits or in the pit walls leading to a decrease in the corrosion susceptibility by means of higher repassivation rate.
6. The corrosion behavior, both GBC and Pitting corrosion, of HTHAZ of modified FSS was mainly influenced by the sensitization process which, was eventually, controlled by the mode of metal transfer. S-mode of metal transfer resulted in better corrosion resistance compared to the SC-mode for both types of corrosion. In addition, it was observed that, the corrosion rate of HTHAZ of both the types were more or less compatible with the corrosion resistance of 308L welds.
7. Finally, from the whole study, three important conclusive statements can be drawn, i.e., among the modes of metal transfer; S-mode, in general, had better performance than SC-mode against GBC in the welds and HTHAZ. Pitting corrosion of welds and HTHAZ is exclusively influenced by the Cr_{eq}/Ni_{eq} ratio and S-mode, respectively. Between the two filler wires, corrosion resistance of 308L welds had close proximity with the HTHAZ, although, 316L welds had much lower susceptibility toward both types of corrosion.

Acknowledgments This work is supported by the Council of Scientific and Industrial Research (CSIR), New Delhi, India. The authors would like to thank Mr. Sunil Sisodia, DGM (Quality), Salem Steel Plant, SAIL, Tamil Nadu, India, for providing the experimental materials and Mrs. D. Kanchanamala of IIT Madras, India, for her assistance in TEM work.

References

1. Meyers AM, du Toit M (2001) Weld Res Suppl 80:275
2. Silva Cleiton C, Faria Jesualdo P, Miranda Helio C (2008) Mater Charact 59:528
3. Fritz JD, Franson IA (1997) Mater Sel Des 57
4. Lippold JC, Kotecki DJ (2005) Welding metallurgy and weldability of stainless steel. Wiley, Hoboken
5. Hisamatsu Y, Ogawa H (1977) Iron Steel 63(5):585

6. Shanmugam K, Lakshminarayanan AK, Balasubramanian V (2009) *J Mater Sci Technol* 25(2):181
7. Kotecki DJ (2005) *Weld J* 84:14
8. Gooch TG, Davey TG (1984) Proceedings of the inaugural international conference. Johannesburg, South Africa, pp 209–229
9. Kim JK, Lee BJ, Lee BH, Kim YH, Kim KY (2009) *Scr Mater* 61:1133
10. Kim JK, Kim YH, Lee JS, Kim KY (2010) *Corros Sci* 52:1847
11. Tuthill AH (2005) *Weld J* 5:36
12. Sedriks AJ (1996) *Corrosion of stainless steels*, 2nd edn. Wiley, New York
13. White WE (1992) *Mater Charact* 28:349
14. Bojinov M, Fabricius G, Laitinen T, Makela K, Saario T, Sundholm G (2001) *Electrochim Acta* 46:1339
15. Cui Y, Lundin Carl D (2005) *Mater Lett* 59:1542
16. Cui Y, Lundin Carl D (2007) *Mater Des* 28:324
17. Bond AP (1969) Transactions of the Metallurgical Society of American Institute of Mining, Metallurgical, and Petroleum Engineers, 2127
18. Demo JJ (1971) *Corrosion* 27(12):531
19. Bilmes PD, Llorente CL, Saire Huaman L, Gasssa LM, Gervasi CA (2006) *Corros Sci* 48:3261
20. Lu BT, Chen ZK, Luo JL, Patchett BM, Xu ZH (2005) *Electrochim Acta* 50:1391
21. Macdonald DD, Ismail KM, Sikora E (1998) *J Electrochem Soc* 145:3141
22. Zumelzu E, Sepulveda J, Ibarra M (1999) *J Mater Process Technol* 94:36
23. Dadfar M, Fathi MH, Karimzadeh F, Dadfar MR, Saatchi A (2007) *Mater Lett* 61:2343
24. Du Toit M, Van Rooyen GT, Smith D (2006) *IIW Doc IX-H-640*
25. Greeff ML, Du Toit M (2006) *Weld J* 85:243 s–251 s
26. Mukherjee M, Pal TK (2012) *Metall Mater Trans A* 43A:1791
27. Lowke JJ (2009) *J Phys D Appl Phys* 42:1
28. Ghosh PK, Devakumaran K, Pramanick AK (2010) *Weld J* 89:43s
29. Brooks JA, Thompson AW (1991) *Int Mater Rev* 36:16
30. Elmer JW, Allen SM, Eagar TW (1989) *Metall Trans A* 20A:2117
31. Pryds NH, Huang X (2000) *Metall Mater Trans A* 31A:3155
32. Lee JH, Kim HC, Jo CY, Kim SK, Shim JH, Liu S, Trivedi R (2005) *Mater Sci Eng, A* 413:306
33. Li JY, Sugiyama S, Yanagimoto J (2005) *J Mater Process Technol* 161:396
34. Ferrandini PL, Rios CT, Dutra AT, Jaime MA, Mei PR, Caram R (2006) *Mater Sci Eng, A* 435:139
35. Charlas (1992) Proceedings of the conference on application of stainless steels'92. Stockholm, Jernkontoret, pp 1108–1121
36. Kerr HW, Kurz W (1996) *Int Mater Rev* 41(4):129
37. Kah DH, Dickinson DW (1981) *Weld J* 60:135s
38. Kim JK, Kim YH, Lee Bh, Kim KY (2011) *Electrochimica Acta* 56:1701
39. Di Schino A, Barteri M, Kenny JM (2003) *J Mater Sci* 38:3257
40. Ravindranath K, Malhotra SN (1995) *Corros Sci* 37:121
41. Gunn RN (ed) (1997) *Duplex stainless steels: microstructure, properties and applications*. Abington Publishing, Cambridge
42. Lula RA, Davis JA (1978) Intergranular corrosion cracking in 12% Cr ferritic stainless steels. In: Stegerwald RF (ed) *Intergranular corrosion of stainless alloys*. ASTM STP 656, pp 233–247
43. Weber L, Uggowitzer PJ (1998) *Mater Sci Eng, A* 242:222
44. Chen L, Tan H, Wang Z, Li J, Jiang Y (2012) *Corros Sci* 58:168
45. Pardo A, Merino MC, Coy AE, Viejo F, Arrabal R, Matykina E (2008) *Corros Sci* 50:1796
46. Wranglen G (1974) *Corros Sci* 14:331
47. Kaneco M, Isaacs HS (2002) *Corros Sci* 44:1825
48. Ilevbare GO, Burstein GT (2001) *Corros Sci* 43:485
49. Lu YC, Clayton CR, Brooks R (1989) *Corros Sci* 29:863
50. Tobler WJ, Virtanen S (2006) *Corros Sci* 48:1585
51. Yang Yinhui, Yan Biao, Li Jie, Wang Jia (2011) *Corros Sci* 53:3756